CHAPTER II

THEORETICAL BACKGROUND

2.1 Infrared Absorption Spectroscopy

Infrared (IR) spectroscopy is an absorption measurement of IR light to excite the vibrations of molecules. It is one of many spectroscopic techniques that can be performed to identify compounds or investigate sample compositions. IR light is divided into three regions: far IR (20-400 cm^{-1}), mid IR (400-4000 cm^{-1}), and near IR (4000-12500 cm^{-1}). In the present work, the investigation of the radiation absorption by molecules is held in the mid IR region.

A basis of the absorption of IR light is a transition between energy levels of molecular vibration. When molecules transit from state m to state n, the energy, $\hbar\nu$, of the absorbed IR light is equal to an energy difference, ΔE, between the two states

$$\Delta E = E_m - E_n = \hbar\nu \tag{2.1}$$

where E_m and E_n denote the absolute energies of the state m and n, respectively; $\hbar$ is the Planck's constant, and ν is the frequency of motion. The vibrational transition of molecules originates from the absorption of an electromagnetic radiation while the process is controlled by the electrical dipole moment defined as

$$\left(\mu_q\right)_{mn} = \int_{-\infty}^{\infty} \psi_n \mu_q \psi_m dQ \tag{2.2}$$

where μ_q denotes a transition dipole moment in Cartesian coordinates $\left(q = x, y, z\right)$, ψ_m and ψ_n denote the wavefunctions for the vibrational states m and n, respectively; and Q denotes a normal coordinate. However, absorption of IR light only occurs when the transition is IR active. According to the IR selection rule, the electric dipole

moment is expanded in the Taylor series with respects to Q based on the harmonic approximation. Hence, the series are restricted to the linear terms

$$\mu_q = (\mu_q)_0 + \left(\frac{\partial \mu_q}{\partial Q}\right)_0 Q + \frac{1}{2}\left(\frac{\partial^2 \mu_q}{\partial Q^2}\right)_0 Q^2 + \ldots \qquad (2.3)$$

Since Q has a small value due to a displacement of atoms during the vibration, Q^2 and the subsequent terms in the eq (2.3) are neglected. Substituting the terms up to Q of eq (2.3) into eq (2.2), the equation is rewritten to

$$(\mu_q)_{mn} = (\mu_q)_0 \int \psi_n \psi_m dQ + \left(\frac{\partial \mu_q}{\partial Q}\right)_0 \int \psi_n Q \psi_m dQ \qquad (2.4)$$

The first term in eq (2.4) is zero because ψ_n and ψ_m are orthogonal. Therefore, two IR selection rules are defined based on the quantum mechanics according to the second term while the terms $\left(\partial \mu_q / \partial Q\right)_0$ and $\int \psi_n Q \psi_m dQ$ must be non-zero. The first selection rule is considered based on the nature of the wavefunction that permits the integral to have a value other than zero only when $n = m \pm 1$ holds. Considering Q^2 and the subsequent terms of eq (2.3), if $n \neq m \pm 1$, i.e. the overtone transition in the near IR region, $(\mu_q)_{mn}$ has a value other than zero, although it is small. Hence, only fundamentals are IR active within the harmonic approximation. The second selection rule is based on the symmetry of a molecule. It is obtained from the term of $\left(\partial \mu_q / \partial Q\right)_0 \neq 0$. This relationship indicates that IR absorption only occurs when the certain vibration changes the electric dipole moment. Because eq (2.4) holds for all three Cartesian coordinates, only one non-zero transition dipole moment is sufficient to account for the IR intensity of the normal mode. Therefore, the IR intensity for this transition averaged from over all molecule orientations is expressed by

$$I \propto \left(\frac{\partial \mu_q}{\partial Q}\right)^2 \qquad (2.5)$$

The excitation of vibrational modes by an IR beam passing a sample yields a decrease of source light intensity I_0 as described by the Lambert-Beer law in eq (2.6). The

resulting intensity I of the transmitted light depends on the concentration c of sample molecules, the path length b through the sample, and the absorption coefficient ε according to

$$I = I_0 \cdot \exp(\varepsilon bc) \tag{2.6}$$

2.1.1 Fourier Transform Infrared Spectroscopy

The heart of Fourier transform infrared (FT-IR) instrument is a Michelson interferometer, as illustrated in Figure 2.1. The device consists of two flat mirrors which are perpendicular to each other, and a beamsplitter. The beamsplitter is placed at the intersection of the optical axes defined by the light source, the detector, and the two mirrors. The first mirror is held in fixed position and a second mirror, the so-called "movable mirror", scans back and forth relative to the beamsplitter during the measurements. When the radiation from the IR source incidents on the beamsplitter, it then reflects 50% to the fixed mirror and transmits 50% to the movable mirror. Consequently, the two beams reflected by the two mirrors are recombined via the beamsplitter, and then leave the interferometer to interact with the sample and eventually reach the detector. The movement of the mirrors correlates with the changes of the optical path length. The path difference between the beams traveling to the fixed and movable mirror is, the so-called, the "optical path difference" (OPD) or "optical retardation"(δ). At $\delta = 0$ or "zero path difference"(ZPD), the fixed and movable mirror are equidistant from the beamsplitter, the two beams are perfectly in phase on recombination at the beamsplitter and interfere constructively. At this point, all the light from the IR source reaches the detector, and the intensity is normally large. If the movable mirror is positioned at a distance $\lambda/4$ $(\delta = \lambda/2)$, the beams are out of phase and interfere destructively on recombination at the beamsplitter. At this point, all the light returns to the source and none passes to the detector. At further displacement of the movable mirror by $\lambda/4$ $(\delta = \lambda)$, the two beams are again in phase on recombination at the beamsplitter with the constructive interference. A plot of the light intensity versus δ (in cm), i.e. a function of moving mirror position, is known as the "interferogram", $I(\delta)$. The interferogram of a polychromatic source has a maximum intensity at the ZPD where all the cosine components are in phase, the

so-called "center burst". Apart from the center burst, as the interferogram is getting smaller, the intensity is weak due to the large path difference. The expression for the intensity of the interferogram from a polychromatic source as a function of retardation is described according to

$$I(\delta) = \int_{-\infty}^{+\infty} \left[\frac{B(\nu)[1 + \cos(2\pi\nu\delta)]}{2} \right] d\nu \tag{2.7}$$

The Fourier transformation then converts the $I(\delta)$ information in the interferogram to a plot of intensity versus wavenumber, $I(\nu)$, which allows an easier interpretation. This transformation is expressed mathematically by

$$I(\nu) = \int_{-\infty}^{+\infty} I(\delta)\cos(2\pi\nu\delta)d\delta \tag{2.8}$$

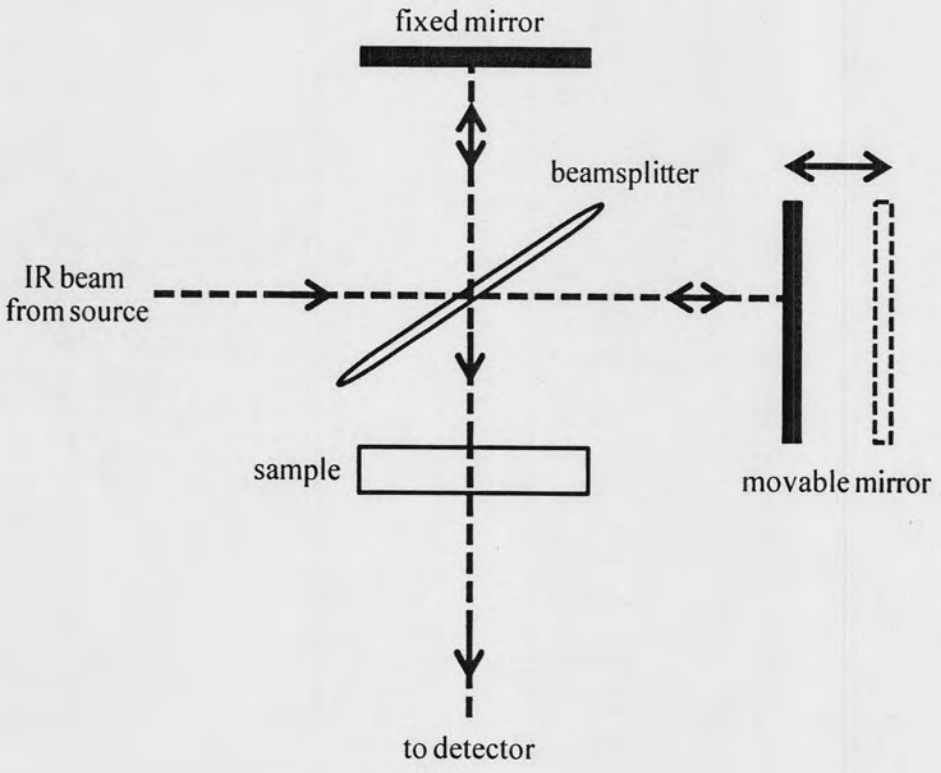

Figure 2.1 Layout of a Michelson interferometer.

2.1.2 Time-Resolved Fourier Transform Infrared Spectroscopy: Step Scan and Rapid Scan Mode

The time-resolved IR spectroscopy has been developed by many scientists [9-12]. The theory of the technique has been discussed e.g., by Griffiths et. al. and Diem [13,14]. The time-resolved technique has been utilised in the FT-IR spectrometry, where the lifetime of the species being studied is shorter than the scan rate of the interferometer. Depending on the scan speed of the movable mirror, the interferometers are used in two different modes: step scan and rapid scan interferometers. The choice of the modes depends on the time scale of the measurements. Within this work the time-resolved FT-IR technique has been employed in combination with potential jumps technique. In such manner, both approaches allow investigations of the kinetics and dynamics of immobilised proteins

2.1.2.1 Time-Resolved Step Scan FT-IR Spectroscopy

A time-resolved method using the interferometer in the step scan mode has been developed by Murphy and Sakai since 1971 [9,10]. The application of a submillisecond step scan FT-IR spectrometer in combination with an ATR SEIRA technique was reported by Osawa et. al. [15] The technique has, then, become popular on the study of biological system. In this work, time-resolved surface enhanced IR absorption (SEIRA) has been applied for the first time to monitor the redox-processes of immobilised proteins.

In a step scan interferometer, the movable mirror is held stationary at each sampling position and driven in step-wise manner to a fixed interferometer position X_n, by means of a stepping motor. At this position, a reaction is initiated and the time-dependence of the spectral changes is measured. Subsequently, the moving mirror is stepped to the next position X_{n+1}, the reaction is repeated and measured again at each mirror positions of the interferogram (Figure 2.2). Therefore, the reaction under study must be repetitive and reproducible. The time interval during the mirror stepping from one sampling position to the next should be kept short because it is the lost time that does not contribute to the observation. The success of the technique depends on the ability of stepping motor to achieve a uniform increase in

retardation for each step. The interferogram signal is produced by integrating the detector output signal during the time interval that the mirror is held stationary. The 3D-representation of the transient data of the whole interferogram is shown in Figure 2.3. After the measurement, the data is rearranged to yield time-dependent interferograms $I(t)$.

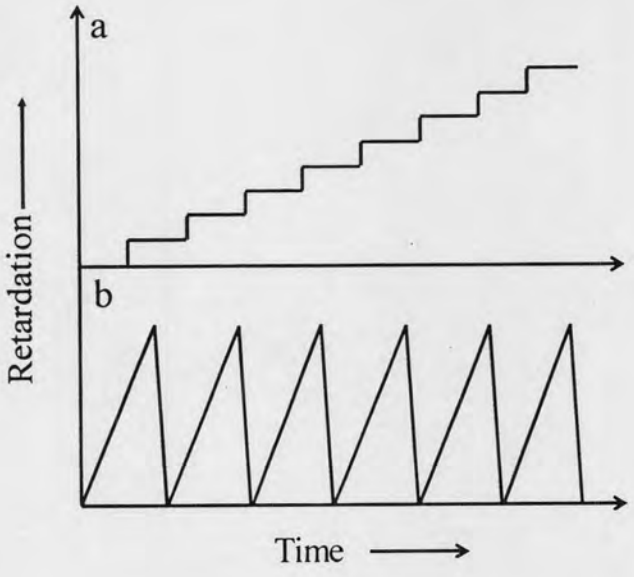

Figure 2.2 The retardation-dependence in time, which is Sed via the interferogram in (a) step-scan and (b) rapid-scan modes.

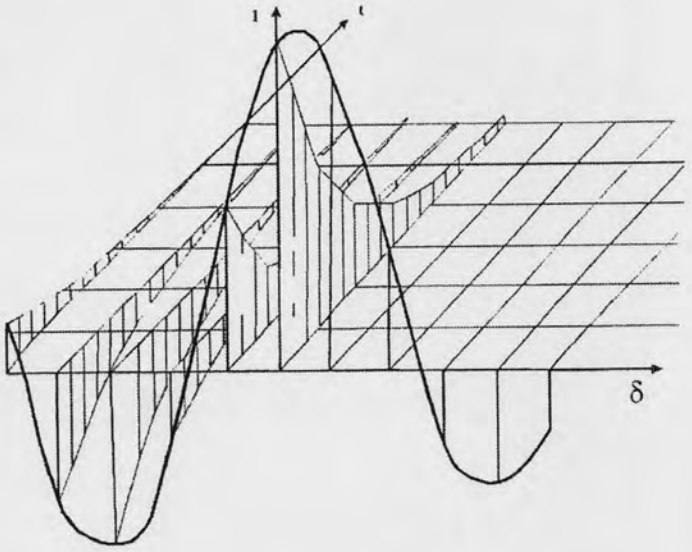

Figure 2.3 A three-dimensional (3D) plot of the intensity (I) versus the optical path difference (δ) and time (t). The interferograms are recorded as a function of time at each sampling positions [16].

2.1.2.2 Time-Resolved Rapid Scan FT-IR Spectroscopy

A similar method for recording time-resolved spectra in a rapid scan FT-IR spectrometer has been developed by Mantz [11,12]. The procedure is quite similar to that of step-scan method excepts that all the data cannot be recorded at a single retardation. In the rapid scan mode, the movable mirror is driven at a constant velocity under computer control, varying the optical retardation continuously (Figure 2.2). The reaction must be triggered at the beginning and the time resolution depends on the difference between two succeeding sampling scans of the interferogram. The rapid scan mode is utilised for the measurement with low- or medium- resolution mid IR absorption spectra, where the interferogram has a high signal-to-noise ratio (SNR). The movable mirror is translated with a sufficient high velocity.

2.1.3 Attenuated Total Reflection Fourier Transform Infrared Spectroscopy

Attenuated total reflection Fourier transform infrared (ATR FT-IR) spectroscopy is a powerful method for surface Sation. The technique has been applied to several biological molecules such as rhodopsin, bacteriorhodopsin, nicotinic acetylcholine receptor, and membrane protein, etc. [17,18]. An obvious advantage of ATR FT-IR is that a thin layer of biomolecules can be deposited on the surface of the internal reflection element (IRE) allowing the investigation of reactivity and reorientation of the biological molecules at interfaces [19,20].

The ATR phenomenon occurs when the light travels from an optical denser medium with the refractive index n_0 and striking the interface at a contact with an optical rarer medium with the refractive index n_1, at an angle of incidence (θ) greater than the critical angle (θ_c), Figure 2.4. The heart of ATR FT-IR technique is the IRE, which has a high refractive index. Typical used materials are Si, Ge, or ZnSe where the refractive indices are 3.4, 4.0 and 2.4, respectively. The choice of the material depends on an inquiring frequency range. In general the IRE configuration includes single reflection variable-angle hemispherical crystals and multiple-reflection planar crystals, as depicted in Figure 2.4.

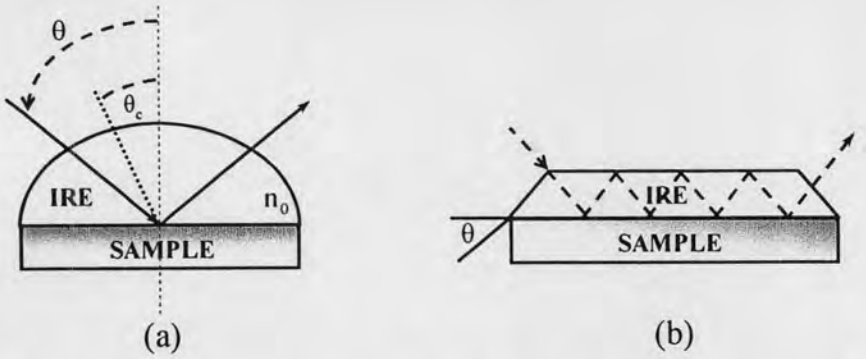

Figure 2.4 Schematic illustration of the beam leading to the total internal reflection phenomenon and IRE configurations for experimental ATR setups: (a) single-reflection variable angle hemicylinder crystal and (b) multiple-reflection planar crystal.

The ATR spectral intensity in absorptance units of a single reflection is given in terms of experimental parameters and material characteristics by the following expression

$$A_p(\theta,\nu) = \frac{4\pi\nu}{n_0 \cos\theta}\int_0^\infty n_1(\nu)k_1(\nu)\left\langle E_z^2(\theta,\nu)\right\rangle dz \qquad (2.9)$$

where p indicates the degree of polarization of the incident beam and k_1 is the absorption index of the sample. The term $\left\langle E_z^2(\theta,\nu)\right\rangle$ is the mean square electric field at depth z. Under the ATR condition, although there is no light traveling across the IRE/sample interface, an electric field is generated at the boundary, the so-called "evanescent field". The field is strongest at the interface and decays exponentially as a function of distance from the interface, Figure 2.5. The rapid decay of the evanescent field is the unique for this technique. In such way, ATR is a powerful tool for surface Sation. The decay pattern of evanescent field can be expressed in terms of the distance from the IRE/sample interface by the following expression

$$\left\langle E_z^2\right\rangle = \left\langle E_0^2\right\rangle e^{-2z/d_p} \qquad (2.10)$$

where $\left\langle E_0^2\right\rangle$ and $\left\langle E_z^2\right\rangle$ are the mean square evanescent fields at the surface and at the depth z in the rarer medium, respectively. The evanescent field at the surface of the rarer medium is determined by the angle of incidence, the refractive indices of two media, and the polarization of the incident radiation.

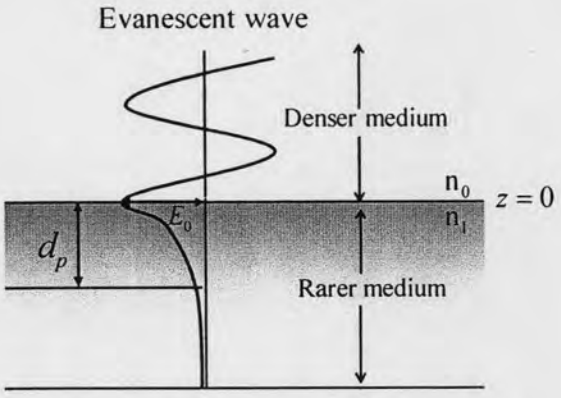

Figure 2.5 The decay pattern of evanescent wave under ATR condition.

The penetration depth, d_p, of the evanescent field is generally defined as the distance within the sample at which the amplitude of the field decreases to $1/e$ of its original value. It is given by the following expression

$$d_p = \frac{\lambda}{2\pi n_0 \sqrt{\sin^2\theta - \left(\frac{n_1}{n_0}\right)^2}} \qquad (2.11)$$

where λ is the wavelength of incident radiation. By altering the angle of incidence, θ, with $\theta > \theta_c$, d_p is consequently varied.

2.1.4 Surface Enhanced Infrared Absorption Spectroscopy

Conventional FT-IR spectroscopy is not a very sensitive spectroscopic technique and requires a high concentration of biomolecules. By means of surface enhanced IR absorption spectroscopy, the sensitivity of IR technique is increased as the intensity of the absorption was improved up to ca. 1000 fold over the normal IR absorption. The first observation of an enhancement of IR absorption by organic molecules adsorbed on silicon substrate was reported in 1980 by Harstein, when a thin metal film was evaporated onto the organic layer [21]. This phenomenon was later denoted as surface enhanced infrared absorption (SEIRA) [22]. The SEIRA effect is of increasing interest for researchers in various areas, especially in the fields of surfaces, interfaces, trace analysis, electrochemistry, and biochemistry. The main

drawback of using this technique in the biological investigation is the strong absorption of IR radiation by bulk solution, especially water. Therefore, an ATR-SEIRA set-up in the Kretschmann configuration (IRE/metal film/solution) is an excellent method suitable for the investigation of biomolecules at the interface with less interference from the bulk solution. SEIRA in the ATR mode has been applied into two different configurations: the "metal-under-layer configuration" (sample/metal/prism) which has been the most widely used in biological applications and the "metal-over-layer configuration" (metal/sample/prism).

The nature and mechanism of SEIRA are similar to those of SERS. The enhancement can be explained based on the electromagnetic (EM) mechanism and chemical effect. Usually, the contribution of the chemical effect is much smaller than that of the EM effect. According to the EM mechanism, a localized plasmon resonance in metal cluster is excited by the incident IR light. A consequence of the plasmon resonance is an increase in the electric field (EF) around the metal. Thus, the total EF is the summation of the incident EF and the enhanced EF induced by plasmon resonance. The enhancement of the EF, F_E, oscillating with frequency ν_0 is given by

$$F_E(\nu_0) = \frac{\left|\vec{E}_0(\nu_0) + \vec{E}_{enh}(\nu_0)\right|}{\vec{E}_0(\nu_0)} \tag{2.12}$$

where $\vec{E}_0(\nu_0)$ and $\vec{E}_{enh}(\nu_0)$ are the incident EF and the enhanced EF, respectively. The enhanced EF decays very sharply within a few molecules distant from the surface. Thus, an absorption enhancement is particularly found for those molecules which are located in close vicinity to the metal surface. The EF is presumably polarized perpendicular to the local surfaces of the metal and thus only vibrations associated with the changes in dipole moments, which are (preferentially) perpendicular to the surface, experience an enhanced absorption. Hence, this effect can be used to determine the molecular orientation of biomolecules including protein. Assuming that the metal particle has a spherical shape with radius a_0, the decrease in the enhancement factor F_{SEIRA} with the distance x from the surface is then given by

$$F_{SEIRA}(d) = F_{SEIRA}(0) \cdot \left(\frac{a_0}{a_0 + x} \right)^6 \qquad (2.13)$$

where $F_{SEIRA}(0)$ is the enhancement factor for molecules directly adsorbed onto the metal surface. SEIRA reveals the enhancement factor between 10^2 and 10^3, whereas SERS has an the enhancement of up to $10^4 - 10^6$ [22]. In addition, an increase of the absorption coefficient, such as caused by the changes of dipole moments of molecules due to chemisorption, will influence the enhancement as well. This effect can be understood in terms of donor-acceptor interactions with the metal surface.

The main factors influencing the magnitude of the enhancement in SEIRA are the morphology (size and shape) of the metal cluster and the particle density of the selected metal cluster films. The metal films which show the SEIRA effect must be discontinuous and consist of small metal cluster with diameters of less than the wavelength of the IR radiation (2.5-15 μm). In practice, SEIRA has been observed on a variety of metals (Au, Ag, Cu, Pt, Sn, Ni, Al and Pb) with varying magnitude of enhancement. Au and Ag exhibit the most intense enhancement and the surface structure is well studied, while the SEIRA observed in the Pt shows a modest intensity enhancement.

Metal films can be formed by several methods, such as vacuum deposition [22], metal sputtering, electrochemical deposition, and chemical (or electroless) deposition [23]. The film morphology can be controlled by the surface structure of the supporting substrate, as well as, by film fabrication conditions (e.g., evaporation rate, temperature, initial reagents etc.). However, the chemical deposition technique, which was utilised in this work, reveals many advantages, i.e. the method is simple, cost effective with a good SEIRA enhancement, and provides a better adhesion of the metal film onto the substrate.

2.2 Proteins

Proteins are complex, high molecular weight organic compounds, which are versatile in structures and functions. They also play a crucial role in living systems, as they are the most abundant cellular components and include enzymes, antibodies, peptide hormones, transport molecules, and components for the skeleton of the cell. Therefore, the study of reactions and reactivity of proteins is one of the most important in the biological research field.

2.2.1 Protein Structure

Proteins are built up from different twenty amino acids. Each amino acid contains an amino group ($-NH_2$), a carboxylic group (-COOH), a hydrogen atom, and a side chain (R) attached to an alpha (α) carbon atom, Figure 2.6. The identity of the particular amino acid depends upon the nature of the R group. Each amino acids in the polypeptide chain are linked by a "peptide bond" as indicated in Figure 2.6. The C-N bond in the polypeptide chains has partial double bond character that makes the peptide bond rigid and planar.

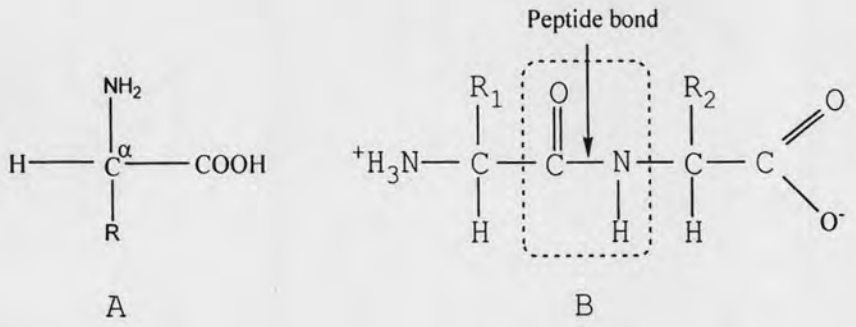

Figure 2.6 A) The structure of an α-amino acid, and B) the peptide bond linking two amino acids.

Four levels of protein structures can be distinguished upon the folding of the polypeptide chains into a 3D-structure. (primary, secondary, tertiary, and quaternary structures). The primary structure of a protein is the linear sequence of amino acid residues that are linked by peptide bonds. The secondary structure is a locally ordered

structure, which is formed mainly by hydrogen bonding within the peptide backbone (Figure 2.7). The most common secondary structure elements in proteins are α-helix and β-sheet (sometimes also called β-pleated sheet or β-strand). The α-helix is a screw-like structure that is stabilised by hydrogen bonds between the C=O and NH groups of the main chain. The C=O group of each amino acid is hydrogen bonded to the NH group of the next fourth residue. Each residue is separated to the next one by 1.5 $\overset{0}{A}$ along the helix axis, which gives 3.6 amino acid residues per turn. The β-sheet structure differs significantly from the helical structure. A polypeptide chain in a β-sheet, which is almost flat compared to the tightly coiled form in the α-helix. It is stabilised by hydrogen bonds between NH and C=O groups in different polypeptide strands, whereas these bonds are found in the same strand for the α-helix. Adjacent chains in a β-sheet can run in the same direction (parallel β-sheet) or in opposite directions (antiparallel β-sheet). Other secondary elements are loops and turns. Turns are U-shaped with three or four residues and stabilised by a hydrogen bond between their end residues. Therefore, the polypeptide folds back by about 180^0 resulting in a compact global shape. Without turns, the protein would be large, extended, and loosely packed. The tertiary structure refers to the spatial arrangement of amino acid residues that are far apart in the linear sequence, resulting mainly from hydrophobic, electrostatic and hydrogen bond between amino acid side chains, and also from the forming of disulfide (S-S) bridges between Cys residues. The quaternary structure is the combination of two or more polypeptide chains in a "multi-subunit" structure. Hemoglobin, for example, consists of two α-helices and two β-sheets in the structure.

Denaturation is the term used to describe the loss of native and higher-ordered structures of protein molecules, thus causing the loss of biological activity. It is mainly involved in the breaking down of interaction in polypeptide chains, which is normally found after the treatment of proteins with strong acids or bases, high concentrations of inorganic salts or organic solvents. Exposure of protein to heat (or irradiation) and high voltages also causes the denaturation of protein.

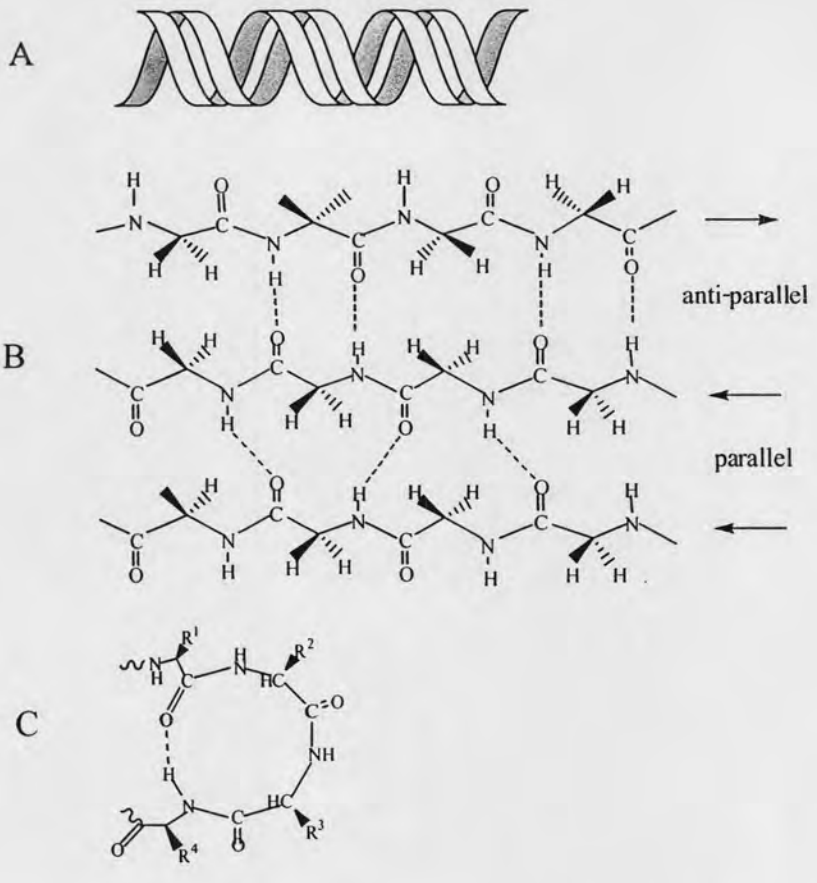

Figure 2.7 The secondary protein structures. (A) Model of the α-helix structure. (B) A three-stranded β-sheet which contains one anti-parallel and one parallel strand. Hydrogen bonds are indicated with red lines (antiparallel strands) and blue lines (parallel strands) connecting the oxygen receptor and hydrogen. (C) A turn structure.

2.2.2 Infrared (Difference) Spectroscopy of Peptides and Proteins

FT-IR spectroscopy is known as a valuable technique for the structural characterization of peptides and proteins. The IR spectra of polypeptides exhibit a number of amide bands that represent different vibrational modes of the peptide backbone in the band frequency range between 1700-1200 cm^{-1}. A good correlation between peptide structure and amide band frequencies has been shown by normal-mode calculations and experimental studies [24]. However, the band assignment is not straight forward due to the huge overlap of peaks representative for the different secondary structures. The Amide I band is found in the range 1700-1600 cm^{-1}, in which the exact band positions are determined by the backbone conformation and the

hydrogen bonding pattern, which is hardly affected by the side-chain. This band results mainly from the C=O stretching vibration of the amide group coupled to the N-H bending and the C-N stretching coordinates. Thus, the huge task is to overcome the difficulty of peak assignments in this region. Another complication is the interference with the intense bending vibration of water (H_2O) and water vapor (rotational-vibration bands). This difficultly can be overcome when samples are measured in D_2O. On the other hand, the bands of water must be subtracted. However, subtraction of the water bands might induce artifacts in the resultant spectrum. Alternatively, one may use a short optical pathlength of 6-7 μm in transmission or employ the ATR technique. With the latter approach, the solution background is significantly decreased, due to the fact that evanescent wave is diminished when penetrating into the solution phase. The Amide II vibrational band is located in the spectral region between 1580-1510 cm^{-1}. It originates mainly from the in-plane N-H bending vibration, strongly coupled with the C-N stretching mode, and it has some small contribution from the C-C stretching vibration, as well. The Amide III region (1320-1220 cm^{-1}) represents the C-N stretching vibration coupled with the N-H in-plane bending and include C-H and N-H deformation vibrations. Further modes of the peptide group are the Amide IV and V, which are not useful to reveal structural information of a protein.

In order to determine small (structural) changes between "two different states" of the protein, difference spectroscopy can be performed, which has been used in our investigations. Instead of measuring the IR absorbance of two different states relative to the corresponding I_0, the single channel spectra of each state can be directly measured. In such way, the intensity changes, (ΔA), between two different states can be determined according to

$$\Delta A = A_2 - A_1 \qquad (2.14a)$$

$$= \left(-\log\frac{I_2}{I_0}\right) - \left(-\log\frac{I_1}{I_0}\right) \qquad (2.14b)$$

$$= -\log\frac{I_2}{I_1} \qquad (2.14c)$$

where A_1 and A_2 are the absorbance of the sample in the first and the second state, respectively. I_1 and I_2 are the intensity passing through the sample in the first and second state, respectively. In such manner, small changes in absorbance intensities of protein reactions in the order of 0.1% can be detected.

2.2.3 Band Assignments of the Protein Secondary Structure in the IR Active Region

Amide I bands are widely used for the examination of the secondary structure due to their strong signal IR intensity. Those, which are centered around 1658-1650 cm^{-1} are generally considered to be a characteristic of α-helical structures. Band overlap of α-helical with β-sheet and turn structures have been also reported to absorb between 1664-1630 cm^{-1}. In H_2O, there also can be an extensive overlap of α-helical structure by random coil structures, which can be distinguished by using D_2O. For the latter solvent, the absorption of the peptide N-D group in the random coil structure is shifted to the lower frequency by about 20 cm^{-1}. Bands characteristic for the β-sheet are mainly observed in the spectral region between 1640-1620 cm^{-1}. The position of these bands is influenced variations in the H-bonding strength and the coupling transition dipoles in different β-strands. Band assignments in this region are further complicated by the overlap with absorptions of β-turn and random coil structures. Amide II bands, however, are not so sensitive to variations in the secondary structure content as the Amide I and III bands, but their analysis increases the accuracy of prediction of the secondary structure. Although the Amide III bands are not disturbed by the absorption band of water and the spectral bands are better resolved compared to the amide I bands, the evaluation of these bands, however, is limited due to the significantly weaker protein signal [24].

2.3 Investigated Protein: Cytochrome c

Cytochrome c (Cyt-c), a monoheme soluble protein, plays a crucial role as a last electron carrier in the mitochondrial respiratory chain by transferring electrons from cytochrome c reductase to cytochrome c oxidase. Most constituents of the respiratory chain are embedded in the inner mitochondrial membrane, or in the cytoplasmic membrane of aerobic bacteria and cells. Cyt-c is a peripheral rather than integral membrane protein. Therefore, it is easy to purify. Another physical property of Cyt-c is a brightly red colored because its heme absorbs strongly in the violet region.

2.3.1 Structure of the Monoheme Cytochrome c

Cyt-c contains a heme group as the active site. The latter consists of porphyrin ring with a tightly bound iron atom held in the central cavity by four nitrogen atoms at the corners of a square. Iron is the redox active part of heme Cyt-c, Figure 2.8.

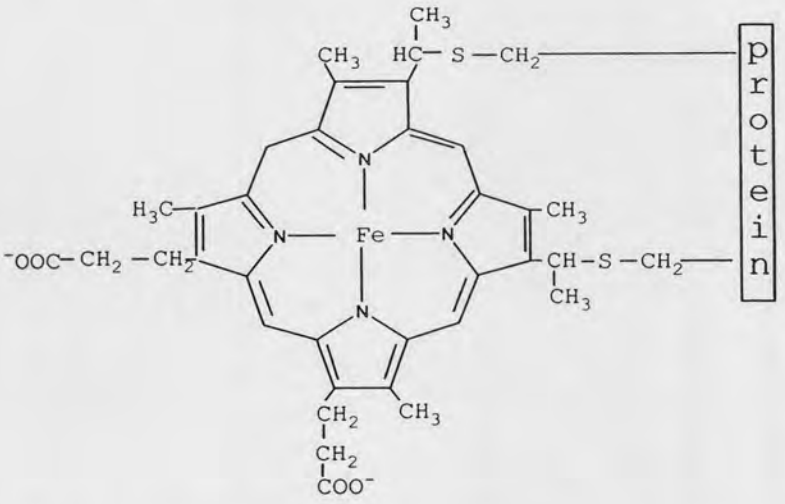

Figure 2.8 Structure of the heme in Cyt-c covalently attached to the protein.

The central iron ion (Fe^{2+}/Fe^{3+}) with 5 or 6 electrons in d-orbital gives rise to two possible arrangements depending on the ligand exchange of the heme. For the case that central iron ion is hexa-coordinated and stabilised by strong ligands, His and Met, all the electrons are located in the low-energy orbitals d_{xy}, d_{xz}, and d_{yz}, which is due to a "strong ligand field" splitting and a large energy difference, Δ_o. Δ_o is the energy

difference between two types of molecular orbitals. This is the so-called the "low-spin" (LS) configuration (Figure 2.9). Conversely, also the high energy orbitals, $d_{x^2-y^2}$ and d_{z^2}, are occupied, if only a "weak ligand field" splitting with a lower Δ_o is induced, that is when the iron center is penta-coordinated. This is the so-called "high spin" (HS) configuration.

The heme group of Cyt-c is covalently linked to the protein via thioether bonds to cysteine residues. The protein surrounds the heme by tightly packed polypeptides of 104 amino acid residues with an excess of positively charged arginine and lysine (K) residues, as well as a small hydrophobic patch, on the surface close to the exposed heme edge. The molecule is about 34 angstrom ($\mathring{A}$) in diameter. The secondary structure of Cyt-c includes three major and two minor helical structures, complemented by strands of polypeptide chains and folded into a rough globular shape in which the heme pocket is formed [25]. Five water molecules have been identified in the structure, three of them are found on the surface and stabilise the conformation of the peptide chain. Models of the globular and the 3D-structures of the Cyt-c in solution are shown in Figure 2.10.

2.3.2 Structural Changes in Cytochrome c

Depending on the different axial ligands, two conformational states, i.e. native B1 and non-native B2 states of Cyt-c have been characterized. The native B1 state refers to a conformation in which His-18 and Met-80 stabilise the six-coordinated LS configuration, the so-called "B1[6cLS]". Perturbation of the native structure lead to the loss of the most labile bound ligand of Cyt-c, Met-80, resulting in the non-native B2 states (three forms). If the sixth coordination site of the iron center is vacant, the five-coordinated HS configuration, "B2[5cHS]" is formed. Otherwise, this site can be occupied either by a water molecule or a strong field ligand (His-33), these are the six-coordinated HS, "B2[6cHS]" and low-spin, "B2[6cLS]", configurations, respectively. However, the B2[6cHS] species only present under certain conditions, e.g. low pH, high ionic strength, and high electric field strength [26,27].

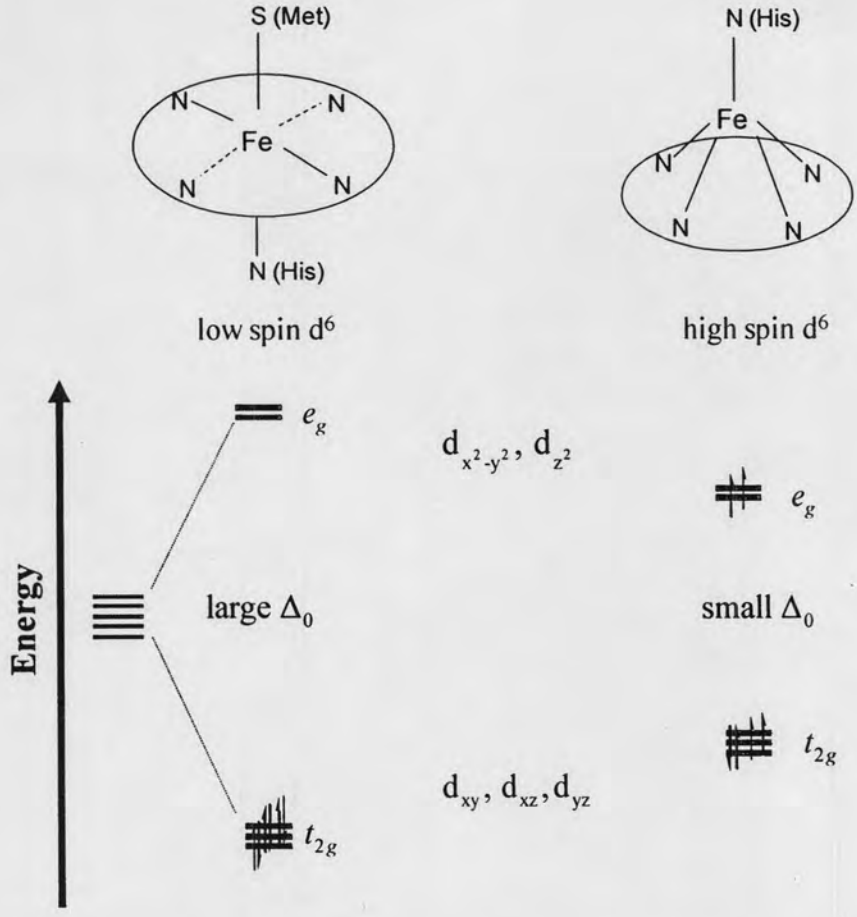

Figure 2.9 Structure of iron complexes in Cyt-c considering the axial ligands and the related energy levels for d_6 iron. The reduced forms of Cyt-c: low-spin (left) and high-spin (right) configurations.

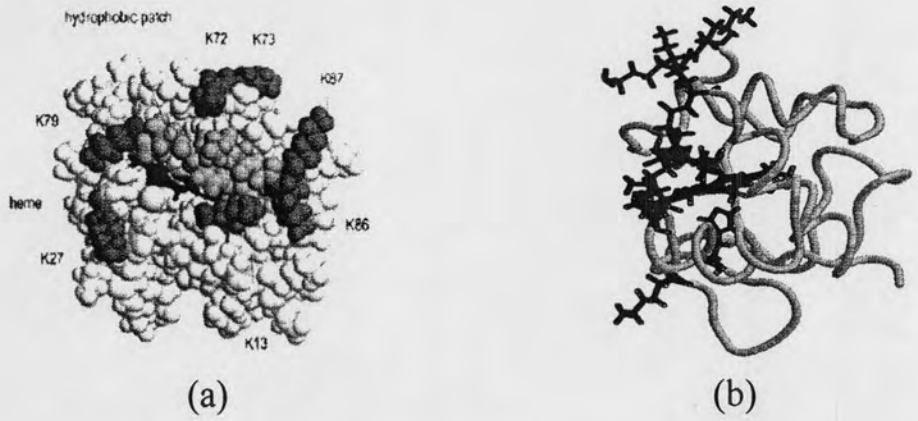

Figure 2.10 The globular (a) and three-dimensional (b) structures of Cyt-c with the front surface view according to the Brookhaven Databank file "1hrc.pdb" [25].

The formation of the non-native B2 structure of the immobilised Cyt-c has been investigated by various spectroscopic techniques, i.e. (surface-enhanced) resonance Raman, UV-Vis absorption, circular dichrorism (CD), and electron paramagnetic resonance (EPR) spectroscopies [27,28]. Depending on the interactions, i.e electrostatic and hydrophobic, at the binding site of the immobilised Cyt-c, two mechanisms of the formation of non-native Cyt-c have been proposed. For the electrostatic binding, Cyt-c is bound to a carboxylate-terminated SAMs coated the electrode via a coulombic interaction between lysine residues and the negative charges on the electrode surface, thereby destabilising the heme crevice, which leads to the formation of B2 state. The amount of B2 increases with raising local electric field (EF) strength. However, the immobilised Cyt-c is preferentially preserved in the native B1 state at high surface coverage of protein [29]. The structural changes of a bound Cyt-c were found to be consistent with those in solution, which may be induced by phospholipids vesicles and micelles. The distribution of native and non-native Cyt-c also depends on the applied electrode potentials as revealed by a study of immobilised Cyt-c on Ag-electrode coated with specific anions [30]. If the interaction is hydrophobic, either in solution, i.e. with the monomeric sodium dodecyl sulfate, or under adsorption on an electrode coated with methyl-terminated SAMs [31], Cyt-c is attached via the small nonpolar patch close to the exposed heme edge. The formation of the B2 state is induced by the movement of the peptide fragment 81-85, which is directly linked to Met-80, inducing the dissociation of Met-80 from the heme crevice. Subsequently, His-33 is preferentially bound and forms the bis-His-coordinated B2[6cLS], while no B2[HS] species was detected. The formation of B2 does not involve major changes of (secondary) structure, but it leads to a modification of the tertiary structure, which was proposed to be involved the movement of the peptide segment 30(20)-49 to transfer His-33(His-26) in proximity to the heme [29]. Due to changes in the ligand pattern and structure of the heme, the redox potentials of B2 states are negatively shifted by ca. 0.40 V with respect to the B1[6cLS]. However, the redox potential of the B1 state is always similar to the value in solution (ca. 0.06 V) [32,33].

2.4 Electrochemical Interfaces

The application of electrochemical methods is here focused on the study of interfacial biological systems. Nevertheless, the application requires an understanding of the principles of electrode reactions and the electrical properties of the electrode/solution interface. At the electrochemical interfaces, reactions take place under conditions that are significantly different from the bulk solution and therefore deserve a special attention.

2.4.1 Electrode Reactions

Reactions at electrodes can be classified as Faradaic and non-Faradaic processes. A Faradaic process is also called a "*charge transfer process*", in which the changes in the redox state of the electroactive species obey the Faraday's law. The Faradaic current is thus a direct measure of the process of a redox reaction, i.e. ET reaction. In contradictory, the non-Faradaic process does not exhibit a charge transfer across an electrode/solution interface, such a process typically occurs when a potential is applied across the double layer, or when the capacitances are changing. In the case of redox process of proteins at electrodes, non-Faradaic reaction steps may include protein reorientation, conformational transitions, proton transfer, ligand exchange of the redox center, or structural changes of the protein [29,34]. Depending on the rate of the individual reaction, either the ET or one of the non-Faradaic reactions may be the rate-limiting step.

2.4.2 Electrode/Solution Interface

The metal electrode possesses a charge which can be controlled by an applied potential. The sheet of the charges at the surface of the metal induces an accumulation of opposite charges next to the metal boundary in the solution hold by electrostatic interactions. Therefore, an electrical potential difference between the electrode (ϕ_m) and the bulk solution (ϕ_s) is created. In order to establish the nature of the electrical potential distributions across the electrode/solution interface, models of an electrical double layer have been developed, as schematized in Figure 2.11. In Helmholtz (HH)

model, the solvated ions arrange themselves, assuming to be a monolayer, in the so-called outer Helmholtz plane (OHP) along the charged electrode surface with a distance limited by the solvation shell. The excess charges on the electrode are balanced with those in solution by ions situated at the OHP. The electrical potential decays linearly between ϕ_m and the OHP (ϕ_{OHP}). The Gouy-Chapman (GC) model utilised the point charges to represent the ions and proposed that the excess charge density in solution is not limited at the OHP, but spread out within the "diffuse layer" by the effect of the Brownian motion in solution. In the diffuse layer, the net charge density decreases with a distance from the electrode in corresponding with the exponential decay of electrical potential from the electrode boundary into the bulk solution (ϕ_s). The Stern model is the combination of the HH and GC models, assuming that the ions closed to the electrode are constrained into a rigid OHP while outside that plane ions are dispersed like in the GC model. The potential sharply drops between the electrode (ϕ_m) and OHP (ϕ_{OHP}), beyond the plane the potential exponentially falls into a value characteristic of the bulk solution (ϕ_s). The further extended model is Grahame model, in which an inner Helmholtz plane (IHP) is identified. Within the IHP, specific adsorbed ions or molecules are directly attached to the electrode.

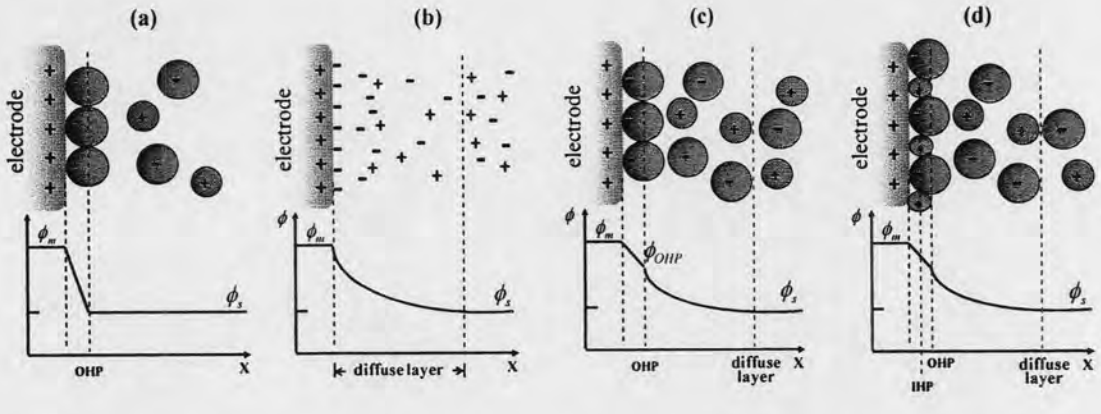

Figure 2.11 Models of the electrical double layer at the electrode/solution interface: (a) Helmholtz, (b) Gouy-Chapman, (c) Stern, and (d) Grahame models.

These simple models can account for electrode reactions of small compounds in direct contact with the electrode. More complex models have to be developed for protein reactions at electrode surfaces. Moreover, direct adsorption of proteins to metal electrodes frequently causes denaturation [5]. Therefore, methods have been developed to prevent direct contact of the protein with the metal.

2.4.3 Modification of Metal Electrode by Self-Assembled Monolayers

Modification of metal electrode with biocompatible molecules provides a flexible system suite for particular biological applications. Formation of biocompatible coating electrode surface can prevent the denaturation of the protein upon direct in contact with the metal electrode. The electrodes can be chemically modified in several different ways, i.e. irreversible adsorption, covalent attachment of a monolayer, and organized assembly techniques. Within the present work, the self-assembly technique has been employed for forming self-assembled monolayers (SAMs) of ω-carboxylalkanethiols on the metal electrode in order to study the electrode reaction of the immobilised protein.

2.4.3.1 Formation of Self-Assembled Monolayers of Organosulfur Compounds on Metal Surfaces

SAMs are defined as a mono-molecular film of a surfactant, which can be prepared using different types of molecules, such as fatty acids, organosilicon derivatives, and organosulfur compounds [35]. However, the organosulfur (e.g. thiol) compounds will be in focus here. The assembling molecule consists of a head, a molecular, and a terminal group, Figure 2.12. The head group is, e.g. thiol, a surface active group that reacts with atoms on the metal electrode. The molecular part consists of alkyl chains, which is used to control the thickness of the molecular film. The terminal group is pointing towards the solution side, and it is a selective group for the adsorption of biomolecules such as DNAs, and protein.

Self-assembly of monolayers is a spontaneous process to form a highly ordered molecular film, upon exposure to the solution, through the strong interaction between

the surface active head group and the metal surface. Stable monolayers are formed easily onto many different metals (Au, Ag, Cu, Pd, Pt). The mechanism of self-assembly of organosulfur compounds on metal surfaces, e.g. Au, was described as an oxidative addition of sulfur bonds to the gold surface in which hydrogen is eliminated. The process is ascribed according to eq (2.15). The S-Au bonding is very strong (ca. 40 kcal/mol), which leads to stable adsorbed monolayers. However, the S-Ag bonding is considered to be stronger [35].

$$X\text{-}S\text{-}H + Au^0 \rightarrow X\text{-}S^-Au^+ + \frac{1}{2}H_2 \qquad (2.15)$$

The adsorption from solution of various n-alkylthiols or substituted analogues on clean electrode surfaces is illustrated qualitatively in Figure 2.12. The main factor that affects the degree of order of monolayers is the interaction among the neighboring alkyl chains of the molecular parts such as the short-range, dispersive, and van der Waals forces. In general, long-chain alkanethiols (≥ ten methylene units) was found to be formed the better order and defect-free monolayers than the short-chain alkanethiols (< ten methylene units) [36]. In such a way, the overall process of SAMs formation is exothermic and characterized by a fast primary chemisorption step which is followed by a slow crystallization process. The latter step requires several hours up to days. According to second harmonic generation investigations, the adsorption kinetics of n-alkanethiols is described by Langmuir's law. After a few minutes the coverage of monolayer on the substrates is almost 90% and an ordered SAM is formed depending on chain length [37].

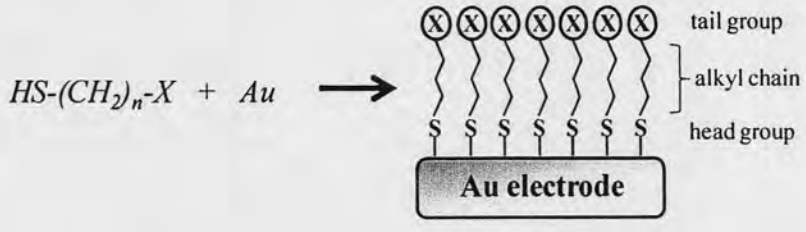

Figure 2.12 Thiols with variable alkyl chain length (n) and tail group (X) form ordered monolayers by self-assembly on gold electrode. $n \geq 1$ and X = e.g. CO_2H, CN, OH, CH_3, pyridine, etc.

2.4.3.2 Properties of Self-Assembled Monolayers of ω-carboxylalkanethiols (C1 to C15)

For the formation of ω-carboxylalkanethiols as SAMs, SH is the active head group and the carboxyl tail group is in contact with the solution (or electrostatic bound to the protein). With this system, the electric field at the interface can be controlled by variation the methylene unit [26]. This enables the study of processes governed by the EF. Some physical and chemical properties of the SAMs are listed in Table 2.1.

Table 2.1 Chain lengths [26] and surface pK_a values of ω-carboxylalkanethiol monolayers as function of SAM-lengths.

SAMs	*chain length* (Å)	*surface* pK_a [a)]
mercaptoacetic acid (C1)	6.3	6.1
mercaptopropionic acid (C2)	7.6	5.3
mercaptohexanoic acid (C5)	11.5	6.0
mercaptoundecanoic acid (C10)	19	7.3
mercaptohexadecanoic acid (C15)	24	7.9

[a)] The surface pK_a's were determined from electrochemical titration [38].

The surface pK_a's of ω-carboxyl alkanethiol monolayers modified electrode slightly increase with increasing alkyl chain length in corresponding to a weaker acidity of the carboxylic acid tail group. The surface pK_a does not influence only the acidity and the interfacial proton transfer reaction of the SAM tail group, but also the electronic state of the SAM surface. Due to only week van der Waals interaction between the alkyl chain of C1-SAM, the monolayer structure is not very compact in this case. Here, the intramolecular interactions of sulfur atoms and carboxylic acid groups are dominant. The stronger interaction between the sulfur atoms and carboxylic groups in the same chain makes the carboxylate more unstable [39]. Thus, the pKa of C1 is larger than that of C2. For $n > 2$, the interaction between sulfur atoms and carboxylic acid groups can be neglected, the influence of intermolecular interaction is dominating.

2.4.4 Interfacial Potential Distribution

The interfacial potential distribution across the biomimicking electrode/SAM/protein/electrolyte interfaces can be described based on a simple electrostatic model [26,40,41] assuming that ions are unable to penetrate into the molecular film. As depicted in Figure 2.13, the interfacial model system consists of a metal electrode at a distance $x = 0$ covered by a SAM of thickness d_C and dielectric constant ε_C. The redox center (RC) is assumed to be in contact with the electrolyte solution at $x = d_C + d_{RC}$ enclosed by the protein matrix with a dielectric constant ε_p. Assuming that the charges in the system are associated with the SAM terminal groups and the RC, the electrostatic potential decays linearly from ϕ_m to the electrostatic binding site (ϕ_C) and significantly increases again from ϕ_C to ϕ_{RC}. Beyond the plane of RC, the potential decays exponentially to the bulk solution (ϕ_s) corresponding to the "GC model" [40].

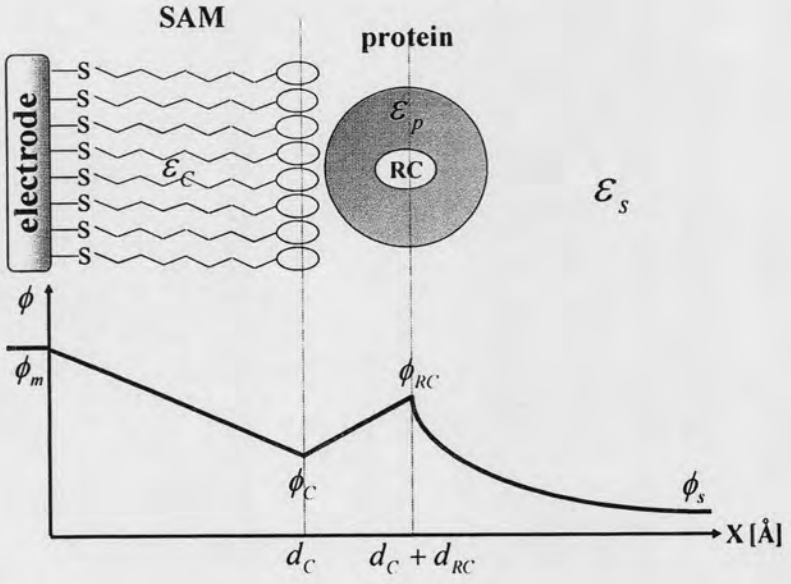

Figure 2.13 Schematic representation of an interfacial potential distribution at electrode/SAM/protein/electrolyte interface.

The potential profile through the interface can be stated in terms of charge densities on the electrode surface (σ_M), at the SAM/protein interface (σ_C), at the RC (σ_{RC}), in the bulk solution (σ_S) and EF strengths throughout the system correspond to

$$E = \begin{cases} 0 & ; x < 0 \\ (\phi_m - \phi_C)/d_C & ; 0 < x < d_C \\ (\phi_C - \phi_{RC})/d_{RC} & ; d_C < x < d_{RC} \\ \kappa(2k_BT/\ell e)\sinh(\ell e\phi_x - \phi_s/2k_BT) & ; x > (d_C + d_{RC}) \\ 0 & ; x \to \infty \end{cases} \tag{2.16}$$

where κ is the inverse Debye length, ϕ_x denotes the potential in the electrolyte solution at position x, ℓ is charge of the electrolyte ions, and e is the elementary charge. Within this model, the net charge densities are neutralized. The potential experienced by the RC of the adsorbed protein $(E_{\exp})$ is associated to the electrode potential (E) by

$$E_{\exp} = E - E_{RC} \tag{2.17}$$

in which E_{RC} is the potential drop at the RC defined as

$$E_{RC} = \phi_{RC} - \phi_S \tag{2.18}$$

Application of Gauss's law, which relates EF and charge densities [41], to the model system in Figure 2.13 yields an expression for the potential drop at the RC according to

$$E_{RC} = \frac{\sigma_C \varepsilon_{RC} d_C + \varepsilon_0 \varepsilon_{RC} \varepsilon_C (E - E_{pzc}) + (d_C \varepsilon_{RC} + d_{RC} \varepsilon_C)\sigma_{RC}}{\varepsilon_0 \left[\varepsilon_C \varepsilon_{RC} + (d_C \varepsilon_{RC} + d_{RC} \varepsilon_C)\varepsilon_S \kappa\right]} \tag{2.19}$$

where ε_0 is the permittivity of vacuum. The EF strength in the SAM region $(0 < x < d_C)$ corresponding to the potential distribution is given by

$$E_{EF} = \frac{\varepsilon_0 \varepsilon_S \kappa E_{RC} - \sigma_C - \sigma_{RC}}{\varepsilon_0 \varepsilon_C} \tag{2.20}$$

In such a way, the EF strength in each region of Figure 2.13, including that at the protein binding site, can be calculated. Previously predictions for carboxyl-terminated SAMs coated Ag electrodes indicated the local EF strengths at the protein binding site in the order of 10^9 Vm^{-1} [26], which is comparable to the values expected in the vicinity of charged phospholipid head groups of biological membranes [42]. Local EF strengths can be also determined experimentally by inserting an appropriate reporter group into the SAM according to the vibrational Stark effect. Specifically, nitrile groups were employed to characterize the diffuse double layer structure at electrochemical interfaces on a subnanometer distance scale showing good agreement with the values obtained by electrostatic theory [43-45].

2.5 Electron Transfer

Numerous essential processes in biology employ ET reactions, e.g., oxygen transport, photosynthesis, respiration, and metabolic syntheses. Understanding ET mechanism is of great importance in the development and operation of biosensors and bioelectronic devices. A general accepted theory of ET was first developed by Marcus [46], and further progressed by others [47-49].

2.5.1 General Considerations

In the electrolyte solution, the ET reaction is divided into three steps. First, an electron donor D and accepter A diffuse together to form an outer-sphere reactant complex $D|A$. In the second step, $D|A$ reorganizes to a transition state in which ET occurs to form a product complex $D^+|A^-$. Finally, this complex dissociates to form the product ions D^+ and A^-. The overall reaction can be written as

$$D+A \underset{k_a}{\overset{k_d}{\rightleftharpoons}} D|A \underset{k_{-ET}}{\overset{k_{ET}}{\rightleftharpoons}} D^+|A^- \xrightarrow{k_s} D^+ + A^- \qquad (2.21)$$

If D and A are held together in a protein matrix, only the second step can occur. Therefore, k_{ET} and (in principle) k_{-ET} can be directly measured.

2.5.2 Homogeneous Electron Transfer

2.5.2.1 Classical Marcus Theory

A potential energy of the initial reactants is a function of many nuclear coordinates (including solvent coordinates), resulting in a multidimensional potential energy surface. The similar surface also holds for the products. In the transition-state theory, a reaction coordinate is introduced such that a one-dimensional energy profile can be considered instead. The Gibbs energy profiles along the reaction coordinate is approximately parabolas as shown in Figure 2.14. The parabola describes the "travel" of reactant R along the reaction coordinate from its equilibrium configuration B to the transition state $Q^{\neq}$, where reactant and product are in the same nuclear configuration. At this point, an electron tunnels from reactant R to product P, and subsequently relaxes to its equilibrium configuration C.

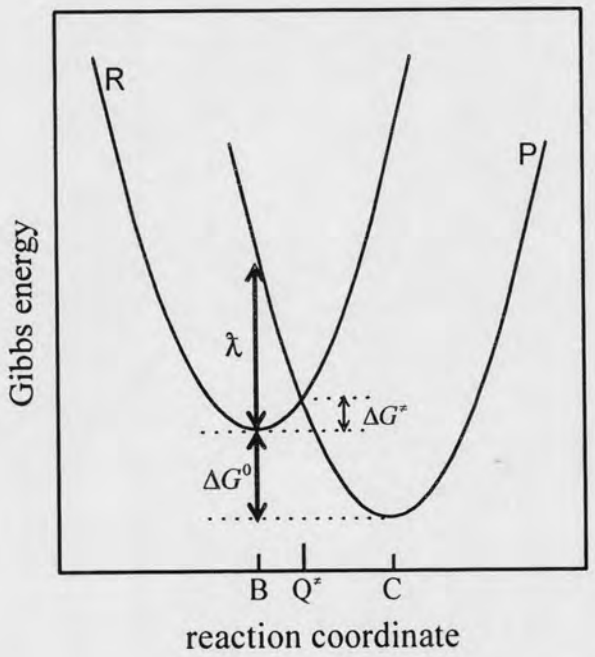

Figure 2.14 Profile of the Gibbs energy surfaces for reactant (R) and product (P).

The ΔG^0 represents the difference in Gibbs energy between equilibrium configuration of reactant and product, $\Delta G^{\neq}$ denotes the Gibbs energy of activation for

the forward ET, and λ is the reorganization energy. According to the classical transition-state theory, the ET rate constant is given by

$$k_{ET} = \kappa_{el} \nu_n \exp\left[-\frac{\Delta G^{\neq}}{k_B T}\right] \tag{2.22}$$

where κ_{el} denotes the electronic transmission coefficient, ν_n is the frequency of the passage (nuclear motion) though the transition state (typically $\nu_n \sim 10^{13}$ s^{-1}). $\Delta G^{\neq}$ is related to the standard reaction Gibbs energy ΔG^0 and to the reorganization energy λ according to

$$\Delta G^{\neq} = \frac{(\lambda + \Delta G^0)^2}{4\lambda} \tag{2.23}$$

Inserting eq (2.23) into eq (2.22) results in the "classical Marcus equation"

$$k_{ET} = \kappa_{el} \nu_n \exp\left[-\frac{\left(\lambda + \Delta G^0\right)^2}{4\lambda k_B T}\right] \tag{2.24}$$

which predicts a maximum of the ET rate for $-\Delta G^0 = \lambda$. As ΔG^0 becomes more negative, i.e., for a highly exergonic reaction, the ET rate will decrease corresponding to the so-called "Marcus inverted region". Experimental evidence was brought for this surprising theoretical prediction [50,51].

ET processes are usually classified into two types according to the magnitude of the electronic transmission coefficient, κ_{el}. The reaction is termed adiabatic if $\kappa_{el} \simeq 1$, i.e. the probability that ET at the transition state occurs is equal to unity. If $\kappa_{el} << 1$, the ET reaction is nonadiabatic, in which although the electron reaches the intersection region $Q^{\neq}$, it only occasionally crosses over to the reactant surface.

2.5.2.2 Reorganization Energy

The reorganization energy, λ, is defined as the change in ΔG^0 when a reactant is distorted to an equilibrium configuration of a product without the transfer

of an electron. λ consists of two contributions as in eq (2.25): inner λ_{in} and outer λ_{out} terms. The term λ_{in} originates from structural differences between the equilibrium configurations of a reactant and product states, and the term λ_{out} arises from the polarization changes in the dielectric solvent environment.

$$\lambda = \lambda_{in} + \lambda_{out} \tag{2.25}$$

λ_{in} is treated harmonically by

$$\lambda_{in} = \frac{1}{2}\sum_{i} f_i \left(r_R^{eq} - r_P^{eq}\right)^2 \tag{2.26}$$

where r_R^{eq} and r_P^{eq} are the equilibrium bond lengths of the reactant and product, respectively; f_i denotes a reduced force constant for the bond vibration, and the summation is taken over all significant intramolecular vibrations. By using a spherical model of reactants and products states, and treating the solvent as a dielectric continuum, the λ_{out} is obtained according to

$$\lambda_{out} = \frac{(\Delta e)^2}{4\pi\varepsilon_0}\left[\frac{1}{2a_D} + \frac{1}{2a_A} - \frac{1}{r_{DA}}\right]\left[\frac{1}{\varepsilon_{op}} - \frac{1}{\varepsilon_s}\right] \tag{2.27}$$

where Δe is the charge transferred in the reaction (usually one), a_D and a_A are the radii of the donor and acceptor, respectively; r_{DA} is the center-to-center distance between the donor and acceptor; ε_{OP} is the optical dielectric constant of the surrounding solvent medium ($\varepsilon_{OP} = n^2$, where n is the refractive index of the medium).

2.5.2.3 Quantum Mechanical Treatment

Classical Marcus theory generally works well for the adiabatic reaction. However, to explain the ET for nonadiabatic reaction, a quantum mechanical approach that accounts for both electron and nuclear tunneling is required. Therefore, quantum mechanical formulations of ET theory have been developed [52-55].

The electronic coupling energy, H_{rp}, corresponds to the overlap of the electronic wave functions of the equilibrium reactant and product states, ψ_R^0 and ψ_P^0, respectively.

$$H_{rp} = \left\langle \psi_R^0 \middle| \hat{H}_{el} \middle| \psi_P^0 \right\rangle \tag{2.28}$$

Where $\hat{H}_{el}$ denotes the electronic Hamiltonian for the system in Born-Oppenheimer approximation. The electronic coupling parameter reflects the exponential decay of electronic wave functions with distance

$$\left|H_{rp}(r)\right|^2 = \left|H_0\right|^2 \exp\left(-\beta\left(r - r_0\right)\right) \tag{2.29}$$

where $\left|H_0\right|^2$ represents the maximum electronic coupling at the van der Waals distance (r_0), r is the distance between the donor and acceptor, and β is an exponential decay coefficient (or tunneling parameter).

The probability of electron transition from an initial energy level in the reactant state to an energy level in the product state is described by the Fermi golden rule which is derived from time-dependent quantum mechanical perturbation theory. It follows for the first-order rate constant for a nonadiabatic ET reaction for reactants fixed in position

$$k_{ET} = \frac{2\pi}{\hbar} H_{rp}^2 FCWD \tag{2.30}$$

where FCWD denotes the Franck-Condon weighted density of states which corresponds to the integrated overlap of reactant and product nuclear wave functions of equal energy, weighted by Boltzmann factors

$$FCWD = \sum_{ij} \left\langle \chi_{Pi}^0 \middle| \chi_{Rj}^0 \right\rangle^2 P(\varepsilon_{Rj}) \delta(\varepsilon_{Pi} - \varepsilon_{Rj}) \tag{2.31}$$

Here, χ_{Pi}^0 and χ_{Rj}^0 are the vibrational wave functions of the equilibrium product state at level i and of the equilibrium reactant state at level j, respectively; ε_{Pi} and ε_{Rj} are the vibrational energies of level i in the product state and of level j in the reactant

state. $P(\varepsilon_{Rj})$ denotes the probability of finding the reactant state in the level j with energy ε_{Rj}, and δ is a Dirac delta function. The summation in eq (2.31) is taken over all internal and solvent vibrational modes, a full quantum formulation of this equation is thus rather complicated.

Different assumptions were introduced to express the Franck-Condon factors. Solvent vibrations usually occur at low frequencies and may be treated classically. Within this approximation, the semi-classical Marcus equation can be written as

$$k_{ET} = \frac{2\pi}{\hbar} H_{rp}^2 \frac{1}{\sqrt{4\pi\lambda_{out} k_B T}} \times \sum_{ij} \left\langle \chi_{Pi}^0 \middle| \chi_{Rj}^0 \right\rangle^2 P(\varepsilon_{Rj}) \exp\left[-\frac{\left(\Delta G^0 + \varepsilon_{Pi} + \varepsilon_{Rj} + \lambda_{out}\right)^2}{4\lambda_{out} k_B T} \right] \tag{2.32}$$

where the summation runs now only over the internal vibrational modes. Other treatments introduce a characteristic frequency which replaces the relevant high-frequency vibrations on the reactant state.

In the high-temperature limit, eq (2.32) reduces to

$$k_{ET} = \frac{2\pi}{\hbar} H_{rp}^2 \frac{1}{\sqrt{4\pi\lambda_{out} k_B T}} \exp\left[-\frac{\left(\lambda + \Delta G^0\right)^2}{4\lambda k_B T} \right] \tag{2.33}$$

and eq (2.33) is equivalent to eq (2.24) with

$$\kappa_{el}\nu_n = \frac{2\pi}{\hbar} \left| H_{rp} \right|^2 \frac{1}{\sqrt{4\pi\lambda k_B T}} \tag{2.34}$$

2.5.3 Heterogeneous Electron Transfer

The same theoretical framework was applied to electrochemical ET reactions. The overall reaction can be in principle described by eq (2.21), the first and last step might be represented by the diffusion of the reactant to and from the electrode or by a conformational change of the reactant to and from a state that is favorable for ET.

Unlike reactions in solution, the electron is transferred from a localised to a delocalised state (or vice versa) in a reaction at a metal electrode interface. The driving force for the ET reaction in solution is given by the difference in Gibbs energy of the donor and acceptor states which is replaced by the activation overpotential in the electrochemical process

$$\eta = E - E^0 \tag{2.35}$$

which is defined by the Nernst equation

$$E = E^0 - \frac{k_B T}{ne} \ln \frac{C_{red}}{C_{ox}} \tag{2.36}$$

Here C_{red} and C_{ox} are the equilibrium concentrations of the reduced and oxidised electroactive species, respectively.

The theoretical background of electrochemical ET reactions is nevertheless not as well established as that of homogeneous reactions and still in progress. Insofar, the investigations have focused mostly on nonadiabatic heterogeneous ET [56]. In analogy to eq (2.32), a transition rate for one electronic level of energy ε in the metal can be expressed as

$$W(\varepsilon,\eta) = \frac{2\pi}{\hbar} \left| H_{rp}(\varepsilon) \right|^2 \frac{1}{\sqrt{4\pi \lambda k_B T}} \exp\left[- \frac{\left(\lambda + \Delta G^0(\varepsilon,\eta) \right)^2}{4 \lambda k_B T} \right] \tag{2.37}$$

Eq (2.37) has to be integrated over all occupied electronic levels in the electrode to yield an expression for the heterogeneous ET rate

$$k_{ET} = \frac{2\pi}{\hbar} \frac{1}{\sqrt{4\pi \lambda_{out} k_B T}} \int d\varepsilon_f(\varepsilon) \rho(\varepsilon) \left| H_{rp}(\varepsilon) \right|^2$$

$$\times \exp\left[- \frac{\left(\lambda + \Delta G^0(\varepsilon,\eta) \right)^2}{4 \lambda k_B T} \right] \tag{2.38}$$

with

$$\left(\Delta G^{0}(\varepsilon,\eta)\right) = \varepsilon - \varepsilon_f - e\eta \qquad \textit{for oxidation} \qquad (2.39a)$$

$$\left(\Delta G^{0}(\varepsilon,\eta)\right) = -(\varepsilon - \varepsilon_f) + e\eta \qquad \textit{for reduction} \qquad (2.39b)$$

Here, $\rho(\varepsilon)$ is the density of states (DOS) of the metal electrode and

$$\rho(\varepsilon)\left|H_{rp}(\varepsilon)\right|^2 = \left|V(\varepsilon)\right|^2 \qquad (2.40)$$

corresponds to the metal-DOS weighted and k-space integrated electronic coupling strength. The Fermi-Dirac distribution function $f(\varepsilon)$ defines the probability that an electronic level of energy ε is occupied by an electron

$$f(\varepsilon) = \frac{1}{1 + \exp\left(\dfrac{\varepsilon - \varepsilon_f}{k_B T}\right)} \qquad (2.41)$$

in which ε_f denotes the Fermi energy.

A relatively simple expression for the ET rate can be obtained by integrating eq (2.38) under several assumptions [57-59]. First, the Fermi-Dirac distribution is replaced by a step function, DOS is considered to be independent of energy and contributions from high and low energy levels $\varepsilon \gg \varepsilon_f$ and $\varepsilon \approx 0$, respectively) are neglected. The rate constant for oxidation and reduction can be then written as

$$k_{ET}^{ox} = A\sqrt{\frac{\pi \lambda k_B T}{e}}\left(1 + erf\frac{e\eta - \lambda}{2\sqrt{\lambda k_B T}}\right) \qquad (2.42a)$$

$$k_{ET}^{red} = A\sqrt{\frac{\pi \lambda k_B T}{e}}\left(1 - erf\frac{e\eta + \lambda}{2\sqrt{\lambda k_B T}}\right) \qquad (2.42b)$$

where the error function is defined as

$$erf(x) = \frac{2}{\sqrt{\pi}} \int_0^{\infty} \exp(-t^2) dt \qquad (2.43)$$

A denotes a constant related to the electronic coupling term $\left|H_{rp}\right|^2$ and thus proportional to the exponential of the distance between the weekly coupled electron donor and acceptor [58].